Journal of Applied Research and Technology

www.jart.ccadet.unam.mx
Journal of Applied Research and Technology 16 (2018) 498-510

Original

Synthesis of hybrid materials, immobilization of lipase in SBA-15 modified with CaO

J. C. Méndez [a], U. Arellano [a], S. Solís [a], M. Asomoza [a,*], V. H. Lara [a], A. J. Padilla [a], J.A. Wang [b]

[a] *Departamento de Química, Universidad Autónoma Metropolitana-Iztapalapa, Av. San Rafael Atlixco No. 186, Iztapalapa, México D.F., México.*

[b] *ESIQIE, Instituto Politécnico Nacional, Av. Instituto Politécnico Nacional, s/n, Col. Zacatenco, 07738, Mexico City, Mexico*

Abstract: Mesoporous silica materials (SBA-15) doped with calcium (Ca) at 1, 3 and 5% w/w were synthesized in order to immobilize candida rugosa lipase (CRL), through the adsorption method. It was found that calcium (Ca) is present as CaO, highly dispersed on the surface of SBA-15, the specific area of SBA-15 decreases on incrementing CaO content. The environmental pH influences the adsorption of CRL due to the polarization of positive charges below the isoelectric point (IEP) whereas the Ca-SBA-15 materials present negative charges. The adsorption model proposed for CRL is about the accessible surface of the material, as this has a size of 7 nm and the Ca-SBA-15 present pores at an interval of 3 nm.

Keywords: Immobilization, lipase, SBA-15, CaO, biomaterials

1. INTRODUCTION

Enzymatic catalysis in both aqueous and nonaqueous environments has gained importance due to its application in industry and medicine (Pogorilyi, Melnyk, Zub, Seisenbaeva, & Kessler, 2016). For the reuse of enzymatic catalysts, it is necessary to carry out immobilization processes, which consist of the deliberate restriction of enzyme mobility. Immobilization of enzymes enables them to remain localized in a defined space region, limited by material or electrostatic barriers, which separate the enzyme physically from the heart of the reaction environment, but stay active, as they are permeable to reactive molecules and products. Additionally, the stability of the enzyme is improved, reducing its consumption, as it can be retired and reused in various reaction cycles (Cai, et al., 2018; Sahoo, Sahu, & Pramanik, 2011; Urrutia, et al., 2018). Enzyme stability depends on its structure, on the method of immobilization and type of medium (Dosanjh & Kaur, 2002). Among the different methods of immobilization, it is important to mention those that act as a result of physical interaction and those that act through chemical bonds (Arroyo, 1998). Adsorption forms part of the first method, involving reversible surface reactions between the enzyme and the supporting material. Since their development, ordered mesoporous silicas have received great attention as: Catalytical support (Taguchi & Schüth, 2005),

* Corresponding author.
E-mail address: mjap@xanum.uam.mx (Maximiliano Asomoza).

Peer Review under the responsibility of Universidad Nacional Autónoma de México.

pharmaceutical administration methods (Ispas, Sokolov, & Andreescu, 2009), rigid bases for other nanostructured materials (Lu & Schüth, 2006), synthesis of nanomaterials (Son, Choi, & Ahn, 2008) and the immobilization of enzymes, due to their morphologic characteristics and structures such as: large specific area, narrow distribution of pore size, hydrophobic character, insolubility in water, chemical and thermal stability, mechanical resistance, adequate particle form, ability to regenerate and nontoxic nature (Dang, Dinh, Nguyen, & Vu, 2010; Lee, Lee, Kim, Kim, & Hyeon, 2011). Lipases (glycerol-ester hydrolases) are enzymes that catalyze hydrolysis of ester bonds present in acilglyceroles. What's more, they can catalyze hydrolysis or synthesis of a wide group of carboxylic esters (Fan, & Qian, 2010; Li, Du, & Liu, 2015; Zheng, Wei, Lan, Zhang, & Wang, 2018). Lipases are soluble enzymes in water that act on insoluble and added substrates which enables them to work together in lipid-water interfaces. Some of the advantages offered by immobilized enzymes include: the possibility of recuperating the enzyme from the reaction environment, obtaining an uncontaminated product with the enzyme, and increasing the operational stability of the biocatalyst (Abbas & Comeau, 2003). One of the methods of immobilization for lipases is the selective adsorption on hydrophobic surfaces that reproduce the interfaces formed by natural substrates of enzymes (Mateo, Palomo, Fernandez, Guisan, & Fernandez-Lafuente, 2007; Urrutiaet al., 2018). In this case, immobilization is produced through an interfacial adsorption mechanism (Reis, Holmberg, Watzke, Leser, & Miller, 2009), based on an enzyme-support activation (Sheldon & Van Pelt, 2013). The development of enzyme supports to synthesize biomaterials has gained great scientific interest. There are diverse types of support reported such as: SiO_2, TiO_2, Al_2O_3, $Ca_{10}(PO_4)_6(OH)_2$ and polymers. There is still great opportunity in methods of synthesis, as the actual methods require sophisticated equipment and are polluting (Rueda et al., 2018). Currently, research is being realized regarding synthesis of supports that could work as immobilizers of enzymes, proteins, peptides and microorganisms; proposing methods of little or no toxicity to health or the environment (Anand & Weatherley, 2018).

In this work SBA-15 materials that had been modified with different contents of Ca were synthesized and the effect of the addition of Ca on adsorption of CRL studied.

2. BASIC CONCEPTS

2.1 SYNTHESIS

2.1.1 Synthesis of SBA-15

SBA-15 was synthesized through tetraethyl orthosilicate (TEOS) in the following way: 4g of Pluronic (P123) were added to 144 mL of a deionized water solution/HC1 1.7 M, stirring for 1 h at 40 °C. Afterwards, 8.6 mL of TEOS were added drop by drop, the resulting mixture being stirred for 2 h at 40 °C and after this, the solvents were evaporated without stirring at 70 °C until obtaining a white solid. The final product was filtered, washed with a water: ethanol 50:50 solution and dried for 24 h at 80 °C. The synthesized samples were calcinated at 550 °C during 24 h.

2.1.2 Synthesis Ca-SBA-15

The Ca-SBA-15 sample with Ca at 3% w/w, was prepared in the following way: 4g of Pluronic were added to 144 mL of aqueous solution 1.7 M of ethanol/HCI and was stirred for 1 h at 40 °C. After this, 8.6 mL of TEOS was added to the previous solution drop by drop, the mix was stirred for 2h at 40 °C. Separately, a solution of 0.27 g of Ca acetate was prepared in 100 mL of ethanol and mixed with the Pluronic/TEOS solution, maintaining stirring during 30 min. Afterwards, 144 mL of deionized water was added drop by drop, maintaining stirring for 24h at 70 °C. Finally, without stirring, the solvents evaporated at 70 °C until a white solid was obtained. The synthesized samples were calcinated at 550 °C over the course of 24 h with air flow. The samples with Ca content of 0.5 and 1.0 % w/w were synthesized with corresponding amounts of calcium acetate in 100 mL of ethanol.

2.2 ADSORPTION OF CANDIDA RUGOSA LIPASE (CRL)

1.2 mg of Candida Rugosa Lipase was dissolved, at room temperature, in 3 mL of phosphate buffer ($NaH_2PO_4H_2O$) at pH 7.5, the mix cools down to 4 °C and 0.5 g of Ca-SBA-15 are added. During the adsorption process, aliquots of 20 µL are taken every 5 minutes for 120 minutes and analyzed through the Biuret method at a wave length of 540 nm, using a double beam spectrophotometer Nanodrop 2000. At the end of 120 min, the solution was filtered and the hybrid material recuperated and freeze dried. The quantity of immobilized CRL was evaluated by way of material balance, with the

Bradford method (Nicolás, Lassalle, & Ferreira, 2017) using the following equation.

$$Pa = C_i - C_f W V \quad (1)$$

Where:

Pa (mg/g) is the immobilized enzyme amount in the support, C_i and C_f are the initial and final concentrations of enzyme (mg/mL), V is the volume of reaction medium/environment (mL), W is the weight of support (g). For the adsorption of CRL, a glycine buffer was prepared at pH 3 and the aforementioned steps were followed.

2.3 CHARACTERIZATION

The X-ray diffraction patterns (XRD) were obtained with a diffractometer Siemens D500. The wide and small angle X-ray scattering patterns were obtained at intervals of 5° to 70° of 2θ and 0.1 to 10° of 2θ, with a step of 0.02° and a measuring time of 2.67 seconds at every point. The specific area was evaluated with the following equipment: Micromeritics ASAP 2000, using the Brunauer-Emmett-Teller (BET) method, to calculate the distribution of pore size the Barrett-Joyner-Halenda method (BJH) was applied, the samples were degasified in a vacuum at 100 °C for 24 h. The FTIR analysis was carried out in an IR affinity equipped with a module ATR Shimadzu, at room temperature. The IR spectra were registered/recorded between 4000 cm^{-1} and 400 cm^{-1}. The TEM images were obtained with a HRTEM Jeol 2100F high resolution microscope, using a field emitter and 200kV of acceleration as a source of illumination; with a resolution of 1.86 A. This equipment has an energy dispersive X-ray (EDX) to carry out elemental analysis and an energy filtration module (EFTEM).

The SEM images were obtained with a Quanta 3D FEG microscope, Brand FEI, with a secondary electron detector (SE) optimized for use in different modes of operation: high vacuum (HV), low vacuum (LV) and environmental mode, as a detector of retro dispersed electrons in their solid state. The determination of zeta potential was carried out with the following equipment: Zeta Meter 3.0+. The previous calibration to each experiment was carried out at -56±3 mV, with a solution of 10% volume in a mix of 10 g/L of natural, fine and highly pure silica (Min-U-Sil) and 10 g/L of sodium chloride.

3. RESULTS AND ARGUMENT

3.1 X-RAY DIFFRACTION

Figure 1 shows the diffractograms at low angle for the SBA-15 and Ca-SBA-15 materials. It observes that the SBA-15 material presents three signals at 1.0°, 1.5° and 2.4° in 2θ respectively, which correspond to reflections (100), (110) and (200), and are associated to a P6mm symmetry, with pores ordered hexagonally (Sun, et al., 2010). In the low angle diffractograms for the materials 0.5Ca-SBA-15, 1Ca-SBA-15 and 3Ca-SBA-15, the intensity of the characteristic signals decreases, which indicates less hexagonal ordering of pores, which is attributed to the inclusion of ions Ca^{2+} in the structure of SBA-15. The inclusion of ions Ca^{2+} in the network of SiO_2 that forms SBA-15 is justified due to the temperature (Kirkendall effect) (Sequeira & Amaral, 2014), resulting in the metals reorganization, this arrangement depends on the ionic radius of the participating metals, on presenting a considerable difference in ionic radius, the distortion of arrangements increases. The ion Ca^{2+} has a radius of 0.99 Å and an ion Si^{4+} of 0.41 Å.

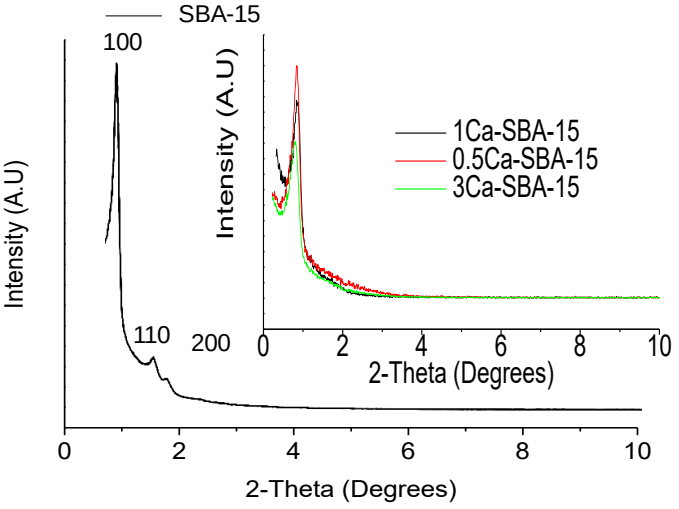

Fig. 1. Diffractograms at small angle for materials SBA-15 and Ca-SBA-15.

Figure 2 shows the wide angle X-ray diffraction patterns for SBA-15 and Ca-SBA-15 materials and observes that at the interval between 15° and 28° in 2θ an intense and wide peak, characteristic of nanocrystalline SiO_2 that forms SBA-15 presenting a hexagonal symmetry that characterizes it. In the diffractograms that correspond to the 0.5Ca-SBA-15, 1Ca-SBA-15 and 3Ca-SBA-15 materials, characteristic peaks of CaO are

observed in 2θ at 31.1°, 36.2° and 54.5°, which correspond with planes (100), (111) and (220) respectively (JCPDS No 741226). The intensity of the characteristic signals of CaO increase according to the content of CaO, which is attributed to the Ca^{2+} ions that are not incorporated into the network and stay on the surface forming CaO in the form of agglomerates.

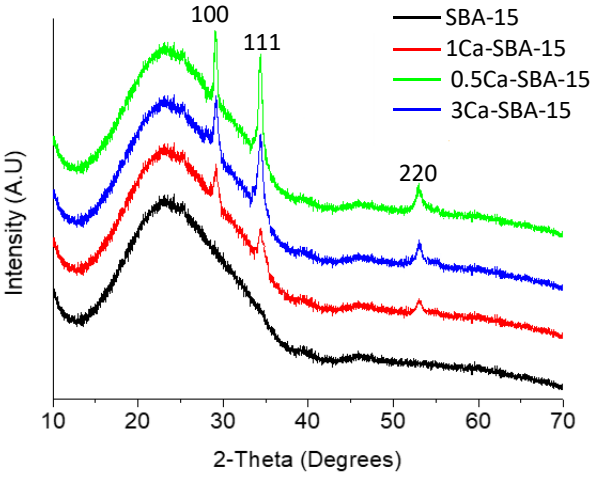

Fig. 2. Wide angle diffractograms for the materials SBA-15 and Ca-SBA-15.

3.2 INFRARED SPECTROSCOPY FTIR

Figure 3 shows the infrared spectra of the calcinated SBA-15 and Ca-SBA-15 materials. It observes a band around 1000 cm^{-1}, that is attributed to the symmetrical stretching vibrations of Si-O-Si, the asymmetrical stretching vibration of Si-O-Si is found at 804 cm^{-1}. The deformation found at 969 cm^{-1} is attributed to Si-OH group. The signal of vibration O-H of the Si-OH group that should appear at 3440 cm^{-1} is not observed, as with the signal corresponding to physically adsorbed water (1648 cm^{-1}), this is attributed to the samples being maintained at a temperature of 100 °C after being calcinated and before the analysis.

There are two small bands at the following intervals: 2900-2931 and 1630-1670 cm^{-1}, which are attributed to the extension vibrations of the OH bond of the occluded water particle molecules in the materials and the residues of C-C coming from the base respectively. The band observed at 450 cm^{-1} is assigned to the flexion vibration of the bond O-Si-O. The most intense bands of the Ca-O bonds are not observed due to their appearance at around 400 cm^{-1} to 290 cm^{-1} (Bhuyan, Selvaraj, & Saiki, 2017).

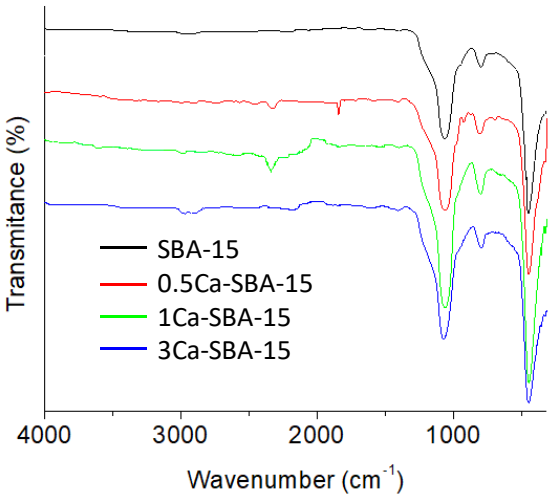

Fig. 3. Infrared spectrum of material SBA-15 and Ca-SBA-15.

3.3 PHYSISORPTION OF N_2

Figure 4 shows the adsorption-desorption isotherms of N_2 materials SBA-15 and Ca-SBA-15, it observes that the materials present type IV isotherms with cycles of hysteresis Type H1 which are characteristic of porous materials that have well-defined cylindric channels, in which occur capillary condensation-evaporation phenomena (Zare, Moradi-Shoeili, Ashouri, & Bagherzadeh, 2017). The differences between the forms of the isotherms is attributed to the content of Ca, as this is found blocking the pores and causing a decrease in adsorbed volume and therefore, the specific area.

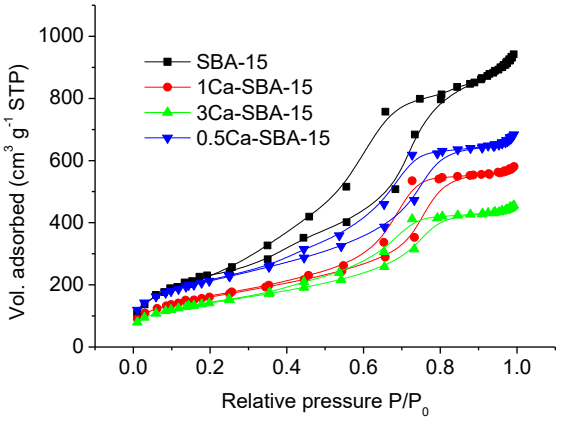

Fig. 4. Isotherms of adsorption-desorption of materials: SBA-15 and Ca-SBA-15.

Table 1 shows the textural properties of SBA-15 and Ca-SBA-15 materials. It observes that SBA-15 presents a specific area of 496 m^2/g with a pore diameter of 3 nm, which is conserved after the incorporation of Ca. The specific area of the material 3Ca-SBA-15 decreases, which

is attributed to the obstruction of pores through the agglomeration of Ca that wasn't incorporated into the SiO_2 structure of the SBA-15, staying in CaO forms dispersed on the surface. The materials 0.5Ca-SBA-15 behave in a similar way, with the Ca blocking the pores and decreasing the specific area. The pore diameter stays constant at 3 nm approximately, which is within the interval for mesoporous materials, according to IUPAC.

Pore volume decreases with the augmenting of Ca content, which is proportional to the decreasing of specific area. These results are attributed to the Ca being found on the accessible surface, in the form of CaO, which cause a decrease in the adsorbed volume of N_2 maintaining a constant pore diameter.

Table 1. Textural properties of materials: SBA-15 and Ca-SBA-15.

Sample	Specific surface area m^2/g	Pore volume (cm^3/g)	Average pore size (nm)
SBA-15	496	0.43	3
0.5Ca-SBA-15	472	0.39	3
1Ca-SBA-15	356	0.35	3
3Ca-SBA-15	219	0.23	3

3.4 SCANNING ELECTRON MICROSCOPY (SEM)

Figure 5 shows SEM images of the materials SBA-15 and Ca-SBA-15. Figure 5a observes a fibrous morphology of the SBA-15 sample, composed of fibers of SiO_2 intertwined with lengths greater than 10 micrometers. This morphology is attributed to the auto-assembly of the micelles of P123 and TEOS, forming short fibers (Grajales, González, & Villa, 2017). Figures 5b, 5c and 5d show the images of materials 0.5Ca-SBA-15, 1Ca-SBA-15 and 3Ca-SBA-15 respectively, observing that the chemical string structure modified itself due to the presence of CaO.

3.5 TRANSMISSION ELECTRON MICROSCOPY (TEM)

Figure 6 shows images of TEM for the materials SBA-15 and Ca-SBA-15. Figure 6a shows the TEM image of SBA-15, with its typical mesoporous hexagonally ordered arrangement (Li, Xu, Jing, Luo, & Chu, 2017). Figures 6b, 6c and 6d correspond to TEM images of the materials 0.5Ca-SBA-15, 1CA-SBA-15 and 3Ca-SBA-15 respectively, where obscure regions are observed that are attributed to the Ca^{2+} not being incorporated into the structure. The excess of Ca^{2+} found homogenously dispersed on the surface of the SBA-15 forms species of CaO. The obscure zones in the images are attributed to the increase of CaO content. The mesoporous hexagonal arrangement is maintained, which indicates that the Ca^{2+} doesn't modify the arrangement of the SBA-15 structure as the largest part of the CaO accumulates on the accessible surface of the material. The ionic radius of Ca^{2+} (0.99 Å), has limited inclusion in the structure of the material SBA-15 due to the difference with the ionic radius of the Si^{4+} (0.41 Å).

3.6 SCANNING ELECTRON MICROSCOPE (SEM) AND ENERGY DISPERSION X-RAY SPECTROSCOPY (EDXS)

Figure 7 shows SEM images and distribution of the chemical composition of the materials Ca-SBA-15, through elemental superficial mapping EDXA. It observes that the materials Ca-SBA-15 are principally formed by Si, O and Ca. Ca^{2+} appears dispersed on the surface of the SBA-15. The dispersion of Ca^{2+} decreases on increasing its content, as it tends to form agglomerates of CaO, which can be seen in the dense, green colored areas.

3.7 ELECTRON SCATTERING SPECTROSCOPY

Figure 8 shows the emission spectra for the materials Ca-SBA-15. It observes that the elements Si, O and Ca are present in the materials, for 0.5Ca-SBA-15 the oxygen content is in a greater proportion, at 57.81%wt, followed by Si at 41.76% wt, and finally Ca at 0.44% wt, which corresponds to the approximate quantity of Ca added.

The materials 1Ca-SBA-15 and 3CA-SBA-15 show a similar trend, approximating to the percentage of added Ca weight, 1.08 and 2.93 % wt respectively.

3.8 ADSORPTION KINETIC

Figure 9 shows the percentages of adsorption, with a solution of 0.4 mg/mL of CRL, in the materials SBA-15 and Ca-SBA-15 at pH 3.5 in glycine buffering solution. At 120 minutes it observes that the materials SBA-15, 0.5Ca-SBA-15, 1Ca-SBA-15 and 3Ca-SBA-15 reach 34, 58 and

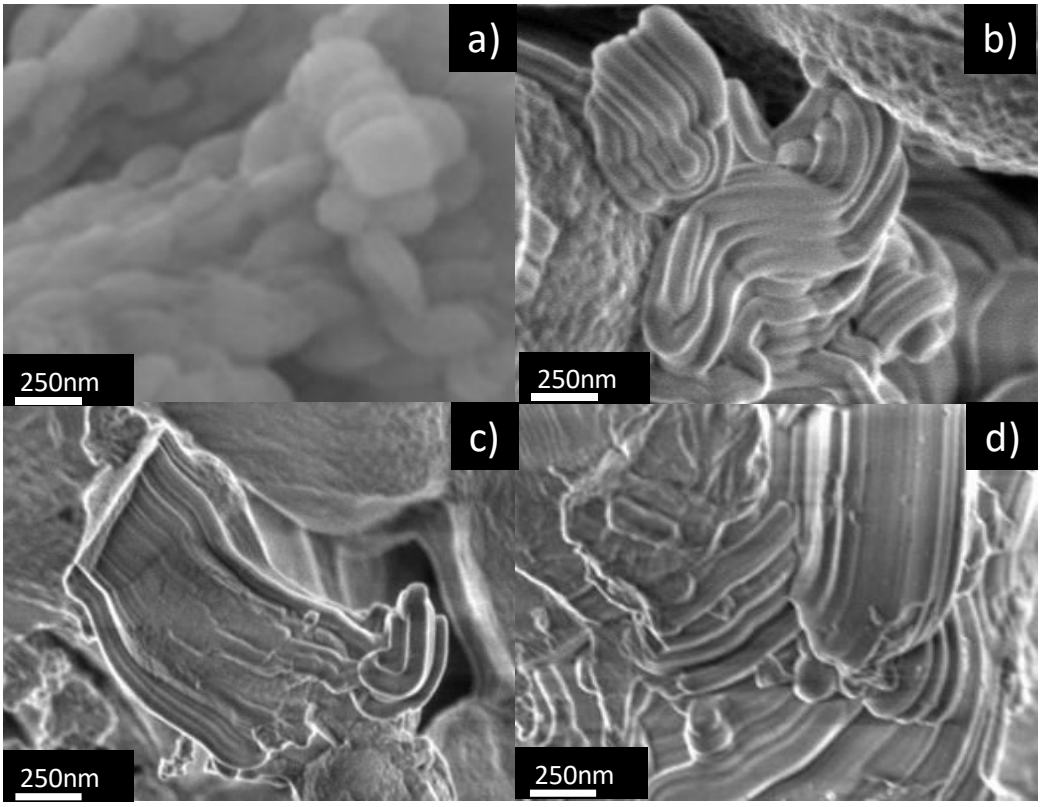

Fig. 5. SEM image of materials where a) SBA-15, b) 0.5Ca-SBA-15, c) 1Ca-SBA-15 and d) 3Ca-SBA-1.

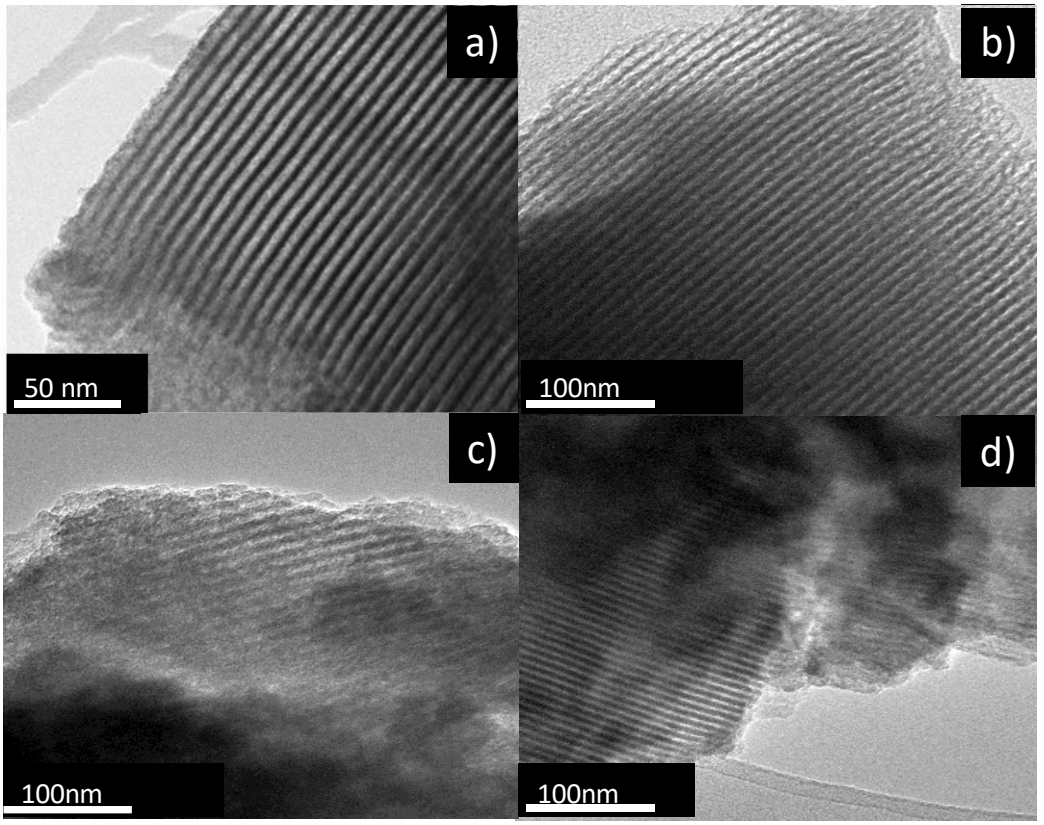

Fig. 6. TEM image of the materials, where a) SBA-15, b) 0.5Ca-SBA-15, c) 1Ca-SBA-15 and d) 3Ca-SBA-15.

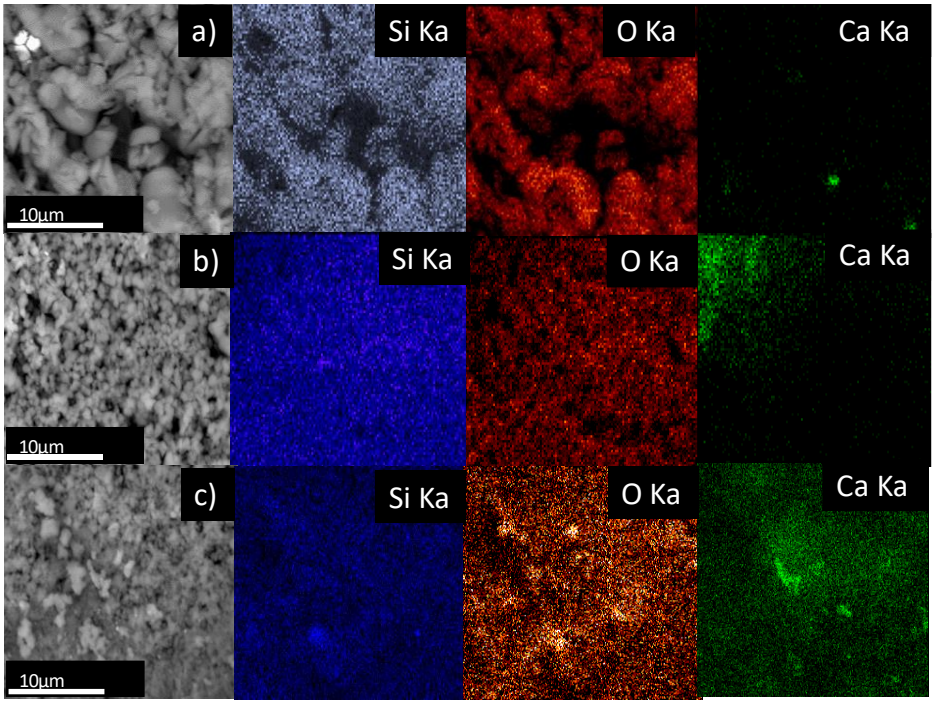

Fig. 7. Images of elemental distribution of material, where a) 0.5 Ca-SBA-15, b) 1Ca-SBA-15 and c) 3Ca-SBA-15.

66 % adsorption of CRL respectively. This behavior is attributed to the pH 3.5 of the medium being lower than the isoelectric point where the enzyme presents positive charges and the material Ca-SBA-15 presents negative charges. Negative charges in the materials with calcium increase on augmenting the content of Ca, which is attributed to the CaO species being dispersed on the surface, in turn promoting densities of negative charge. Calcium which is not incorporated into the silica structure stays distributed on the surface of SBA-15, interacting in the form of Ca agglomerates.

These agglomerates likely interact with the solid, promoting negative charges which permit the adsorption of CRL. The size of the CRL is approximately 7nm (calculated by Protein Calculator v3.4), which impedes penetration in the porosity of silica. The CRL only interacts on the superficial area of mesoporous material, where it can anchor to the irregular surface through interaction of charges.

Figure 10 shows the kinetic analysis of CRL adsorption in the materials SBA-15 and Ca-SBA-15 at pH 3.5, it observes that the adsorption follows a pseudo first order. The affinity for the CRL increases with CaO content. Table 2 shows the kinetic parameters of CRL adsorption in materials SBA-15 and Ca-SBA-15 at pH 3.5, calculated through linearization of the kinetic $\ln(C_0/ C)$ /time, it observes that the CRL adsorption is greater in the material 3Ca/SBA-15 followed by 1Ca/SBA-15 and finally SBA-15. The adsorption half life time of CRL at pH 3.5 is 81, 69 and 60 minutes for SBA-15, 0.5Ca-SBA-15 and 1Ca-SBA-15 respectively. This time decreases to 49 minutes in the case of 3Ca-SBA-15, which is attributed to the increase of calcium in Ca-SBA-15. The velocity K constant is affected by diverse factors including average pH, CaO content, morphological differences, dispersion of CaO in the mesoporous material SBA-15. There is a direct relationship between adsorption percentage for CRL and velocity constant in the reaction conditions studied and for this reason on greater presence of negative charges, the adsorption is realized in a faster fashion.

Figure 11 shows the adsorption percentages for the solution with 0.4 mg/mL of CRL in the materials SBA-15 and Ca-SBA-15 at pH 7.5 in phosphate buffering solution. At 120 minutes, it observes that the SBA-15, 0.5Ca-SBA-15, 1Ca-SBA-15 and 3Ca-SBA-15 reach 54, 38, 36 and 26% of adsoption, respectively. These results are attributed to the average pH, due to the CRL presenting a nucleophilic character in these conditions (high affinity for positive charges) which decrease the affinity for materials Ca-SBA-15 and increase the affinity for SBA-15.

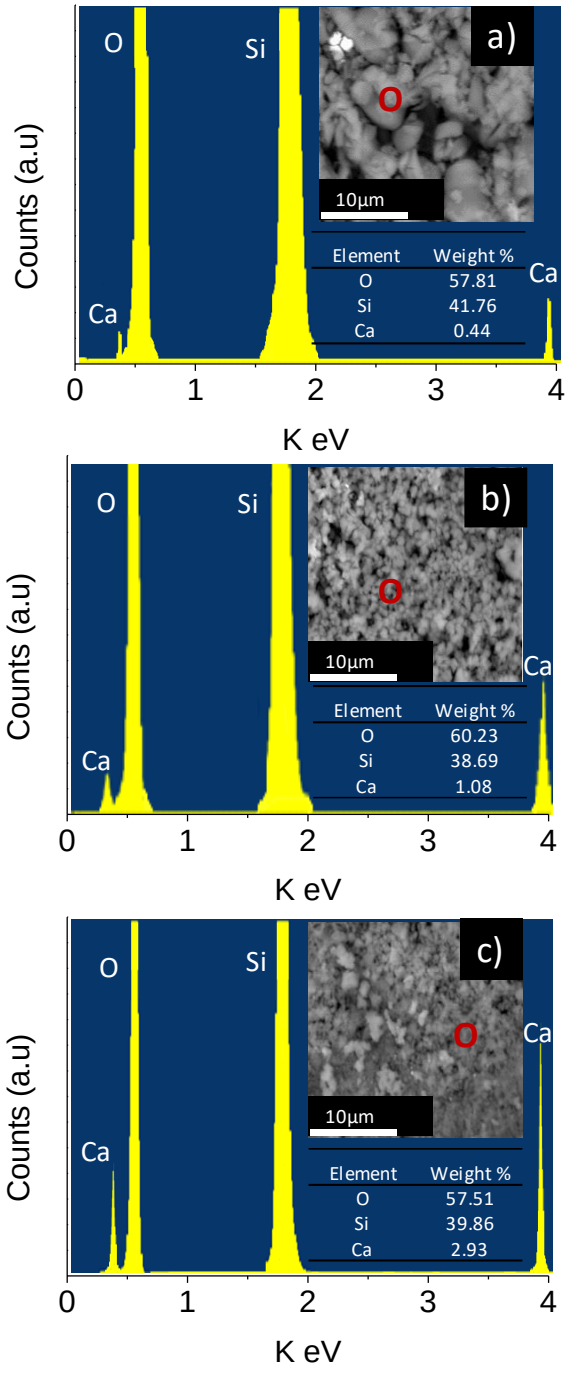

Fig. 8. EDX of nanomaterials where a) 0.5Ca-SBA-15, b) 1Ca-SBA-15 and c) 3Ca-SBA-15.

Table 2. Kinetic constants of CRL adsorption in materials SBA-15 and Ca-SBA-15 at pH 3.5.

Material	$t_{1/2}$(min)	K(min^{-1})
SBA-15	81	0.0086
0.5Ca-SBA-15	69	0.01
1Ca-SBA-15	60	0.0116
3Ca-SBA-15	49	0.0141

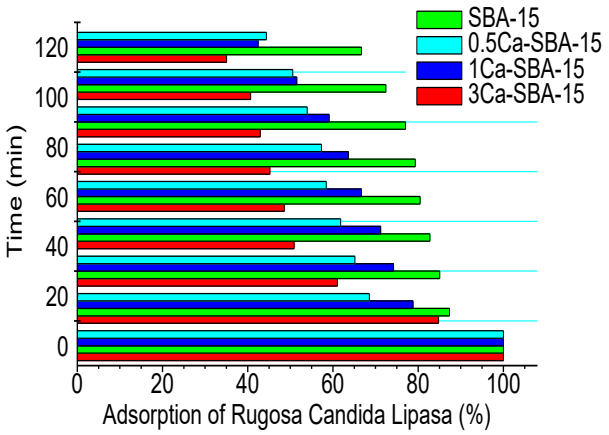

Fig. 9. Adsorption of CRL in the materials SBA-15 and Ca-SBA-15 at pH 3.5.

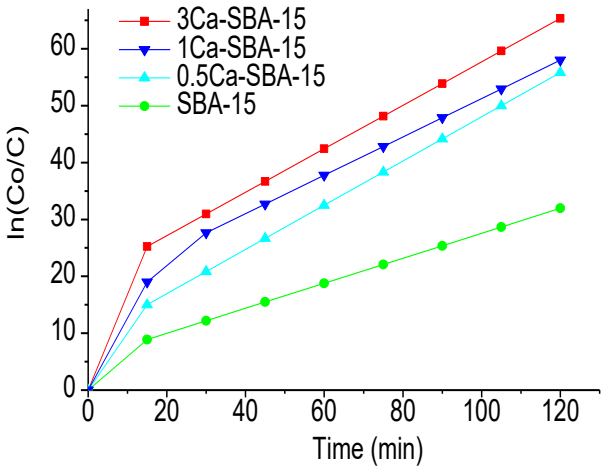

Fig. 10. Kinetic analysis of CRL adsorption in materials SBA-15 and Ca-SBA-15 at pH 3.5.

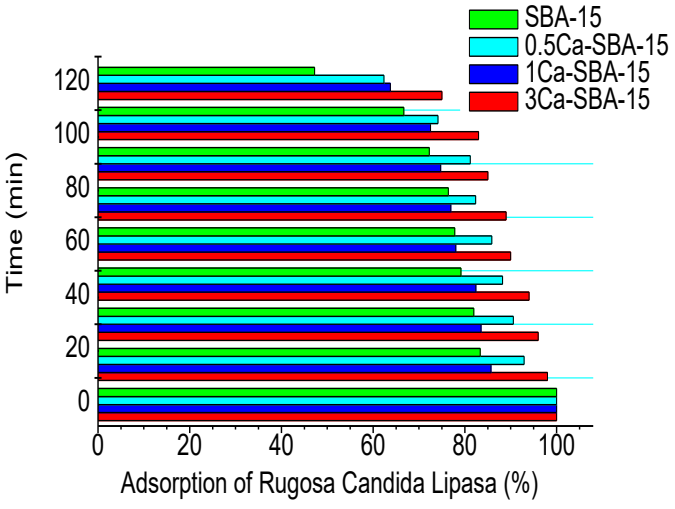

Fig. 11. CRL adsorption in materials SBA-15 and Ca-SBA-15 in pH 7.5.

Figure 12 shows the kinetic analysis of CRL adsorption in materials SBA-15 and Ca-SBA-15 at pH 7.5. It observes that the adsorption follows a pseudo-first order. In these conditions, the CRL adsorption by the materials is lower, it observes that the calcium content function decreases, which is caused by the negative charges presented by CRL in this environment. In these conditions, the CRL augments its affinity for SBA-15 due to its presenting of less negative charges.

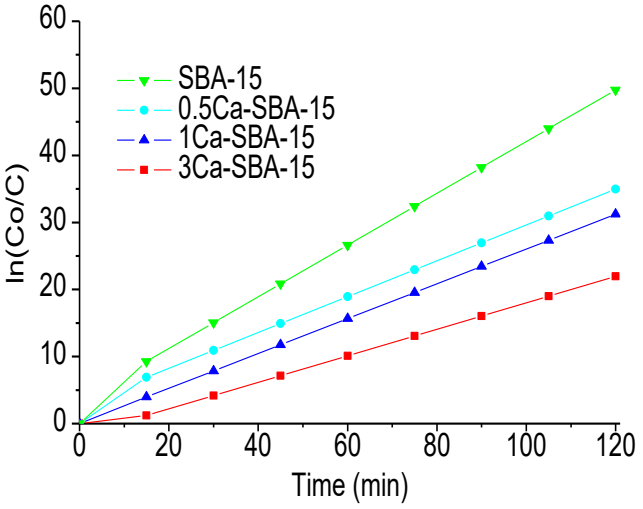

Fig. 12. Kinetic analysis of CRL adsorption in materials SBA-15 and Ca-SBA-15 at pH 7.5.

Table 3 shows the kinetic parameters of CRL adsorption in the materials SBA-15 and Ca-SBA-15 at pH 7.5, calculated by linearization of the kinetic $\ln(C_0/C)$ /time, it observes that the CRL adsorption is favored by the SBA-15, followed by 0.5Ca-SBA-15, 1Ca-SBA-15 and finally 3Ca-SBA-15. The half-life time of CRL adsorption at pH 7.5 is 78, 80 and 87 respectively for SBA-15, 0.5Ca-SBA-15 and 1Ca-SBA-15. This time increases to 92 minutes for 3Ca-SBA-15, which is attributed to the Ca presenting negative electrostatic charges on the mesoporous material.

Table 3. Kinetic constants in CRL adsorption of materials SBA-15 and Ca-SBA-15 at pH 7.5.

Material	$t_{1/2}$(min)	K (min^{-1})
SBA-15	78	0.0089
0.5Ca-SBA-15	80	0.0087
1Ca-SBA-15	87	0.0080
3Ca-SBA-15	92	0.0075

3.9 ENERGY FILTERED TRANSMISSION ELECTRON MICROSCOPY (EFTEM)

Figure 13 shows images from energy filtered transmission electron microscopy (EFTEM) for material 3Ca-SBA-15 with adsorbed CRL, they observe the chemical species involved, both from the material 3Ca-SBA-15 and the elements that compose the CRL. For this analysis, the nitrogen contained in the CRL is monitored, as 3Ca-SBA-15 doesn't contain nitrogen in its structure. The high density green colored zone observed on the edge of the 3Ca-SBA-15 is attributed to the presence of the nitrogen contained in the CRL. There are also densities observed in C and Si (red and blue colored respectively) which pertain to SBA-15.

3.10 ZETA POTENTIAL (ζ)

The interactions between CRL and the SBA-15 and Ca-SBA-15 particles at pH 3.5 and 7.5 were studied by zeta potential (z), this potential is linked to the isoelectric point (IEP). It is recognized that the IEP of CRL is 4.87 and 2.5 for SBA-15 (Ning, Li, Chen, Liu, & Chen, 2005). Therefore, below and above the IEPs, superficial positive and negative charges are respectively developed (Blanco, Terreros, Fernandez-Perez, Otero, & Diaz-Gonzalez, 2004; Dove, & Rimstidt, 1994).

Table 4 shows the z potentials at pH 3.5 y 7.5 of CRL, SBA-15 and Ca-SBA-15, before and after immobilization. It observes that at pH 7.5, the IEP for adsorption participants is greater, negative charges are presented in the CRL and the negative electrostatic sites in SBA-15 increase with the content of Ca in the material Ca-SBA-15. At pH below the IEP point, (pH 3.5) the CRL and SBA-15 generate positive charges, whereas the electrostatic charge sites of Ca-SBA-15 are negative. These charges increase with the content of Ca. The opposing charges of participants create electrostatic conditions that favor the adsorption whereas uniform charges produce repulsion which results in difficult adsorption (Zhang & Binner, 2008).

4. DISCUSSION

While common, adsorption is a very complicated phenomenon; trying to elucidate the adsorption mechanism between the CRL and SBA-15 and Ca-SBA-15 supports, charge densities, hydrophobia, medium pH

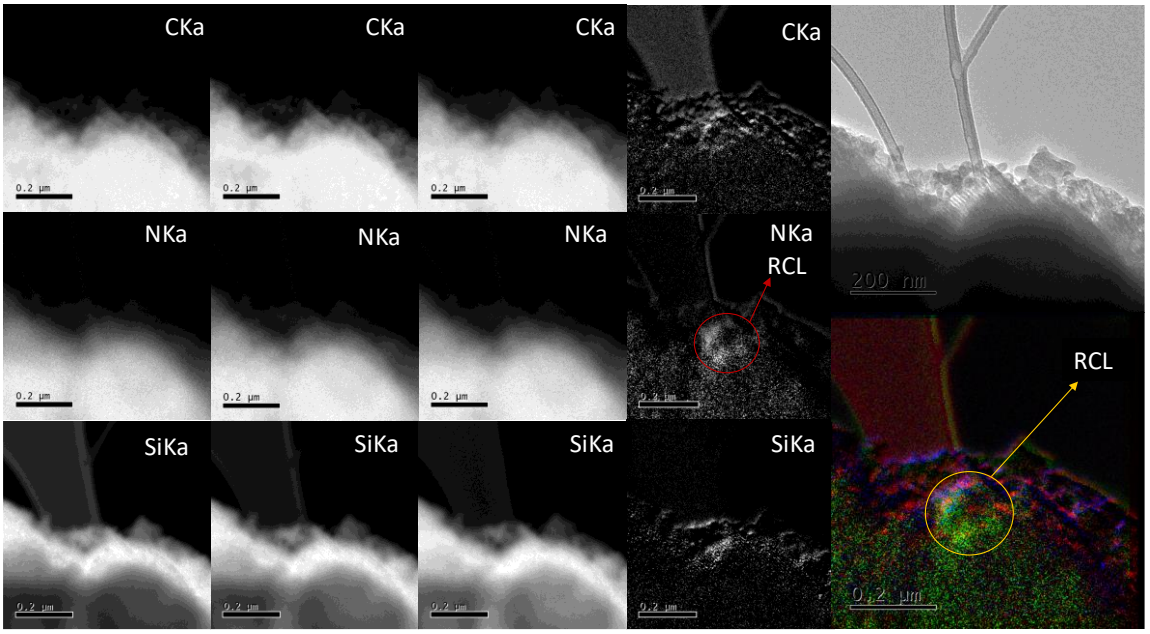

Fig. 13. Energy filtered transmission electron microscopy (EFTEM) 3Ca-SBA-15 with adsorbed CRL.

Table 4. Zeta potential for materials SBA-15, Ca-SBA-15 and CROL before and after immobilization at 25 °C.

Buffer, pH	CRL (mV)	SBA-15 (mV)	CRL						
			SBA-15			SBA-15 (mV)	SBA-15		
			0.5Ca (mV)	1Ca (mV)	3Ca (mV)		0.5Ca (mV)	1Ca (mV)	3Ca (mV)
Glycine 3.5	8.6	14.9	-9.8	-17.7	-42.2	11.8	-0.6	-4.6	-16.8
Phosphates 7.5	-18.8	-24.1	-44.2	-62.0	-84.1	-21.5	-31.5	-40.4	-51.5

and particle size all play a relevant part in the adsorption process. The glycine buffering solution presents an acidic pH, which causes an abundance of protons in the reaction medium and all the functional groups of CRL present positive charges. Therefore, the CRL net charge is (+). As the pH increases, the acidity in the medium gets neutralized, the H^+ decrease and the CRL loses its acidic groups, conserving its amino groups. CRL acquires a dipolar ion state, with charges at both extremes. When the medium acquires basic character, the amino groups lose an H^+ and the CRL acquires charge (-). With the addition of CaO to the material SBA-15, the formation of negative electrostatic charge is promoted, therefore, in the adsorption at pH 7.5 both participants, Ca-SBA-15 and the CRL acquire densities of similar charges which causes the affinity between CRL and Ca-SBA-15 to decrease. In alkaline adsorption conditions the CRL has greater affinity for SBA-15 as it presents sites of opposing electrostatic charges. When adsorption occurs at pH 3.5, the CRL acquires positive charges while the materials with CaO increase the density of the negative electrostatic charge functioning as calcium content, which in turn reflects a greater adsorption of CRL. The adsorption mechanism has been described and used successfully in the case of other enzymes, such as papain and trypsin (Binner, Mcdermott, Yin, Sambrook, & Vaidhyamatham, 2006; Han, Watson, Stucky, & Butler, 2002). The enzymes access to the interior of the SBA-15 pores depends solely on the pore size that should be at least 4 or 5 times greater than the enzymes diameter (Bosley & Clayton, 1994).

As the diameter of the CRL is 7 nm (calculated by protein calculator v3.4) and the pore size determined by the BJH method is around 3 nm, the CRL is unable to access the SBA-15 pores and therefore is found on the surface. Micropores that connect the principal channels are generally small, therefore not influencing the immobilization of the CRL. The specific areas of the materials SBA-15 and Ca-SBA-15 play an important role as they can be hydroxylated in an aqueous medium, the bigger this is, the more OH groups it can absorb. ζ potential reflects the individual properties on the surface of the materials SBA-15 and Ca-SBA-15. Table 4 observes the behavioral changes on the surface when it makes contact with a liquid containing suspended CRL. The influence of the pH causes the CRL to have positive or negative charges on decreasing or increasing the pH respectively. Figure 14 shows the proposed CRL adsorption mechanism in 3Ca-SBA-15, at pH 3.5. It observes that at a pH below the IEP point, the CRL generates positive charges, while the Ca-SBA-15 generate negative charges, these charges increase on incrementing the Ca and because of this adsorption is facilitated when opposing charges present themselves.

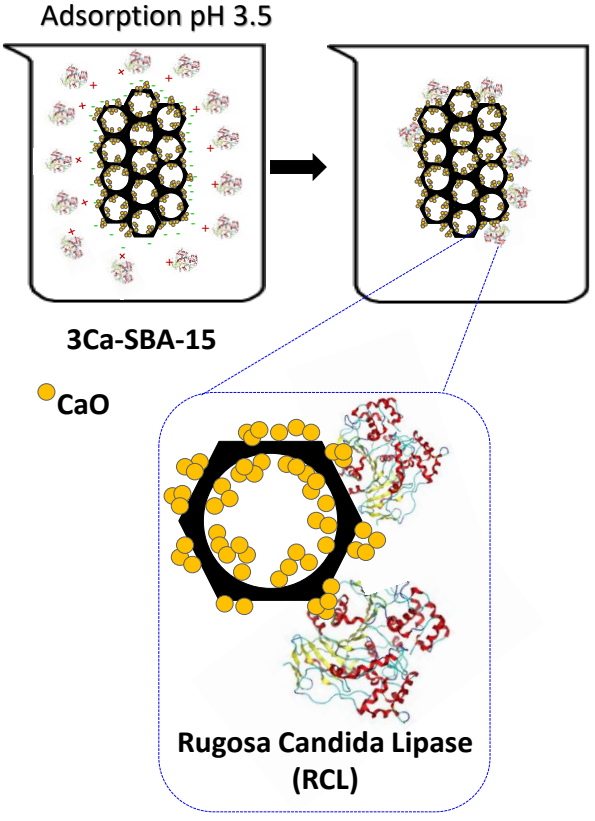

Fig. 14. Proposed scheme of CRL adsorption in 3Ca-SBA-15.

5. CONCLUSIONS

Mesoporous materials with Ca, synthesized in this study through the direct metal incorporation method, presented x-ray diffraction patterns similar to the mesoporous of SBA-15 due to Ca being found in the form of very dispersed microcrystals. Infrared spectroscopy contributed to the identification of functional groups present on the surface of the obtained materials. Scanning electron microscopy enabled the study of the superficial morphology of SBA-15, including its fibrosity which diminishes depending on increase of added calcium. Transmission microscopy enables the identification of typical pore ordering of SBA-15 and justification of the presence of Ca through the EDS technique. The alteration of materials through adding calcium partially destroys their mesoporous, hexagonal structures, which would indicate that the inclusion of Ca^{2+} is minimal in the SBA-15 structure due to the size of the ionic radius in Ca^{2+} being greater than that of Si^{4+}, segregating itself on the largest part of the accessible surface in the form of CaO. The physisorption of nitrogen enables the exploration of the specific area, diameter and pore volume, it observes that the materials with calcium added keep their pore diameter and only the adsorbed N_2 volume decreases, which indicates that part of the added calcium segregates itself on the surface of the mesoporous material in the form of CaO therefore decreasing the specific area. SBA-15 and Ca-SBA-15 were synthesized with adequate characteristics for the adsorption of the CRL. The presence of Ca augments the adsorption of CRL at pH 3.5 and this is due to the fact that calcium acts with opposite charge. The presence of CRL on the surface was determined by the EFTEM technique where the presence of nitrogen is demonstrated to correspond to CRL. Nitrogen is only observed in the CRL, while the elements present in the materials SBA-15 and Ca-SBA-15 are Si, O, Ca and C.

ACKNOWLEDGEMENT

We would like to thank the Catalysis department at UAM-Iztapalapa for their support in the realization of this research.

CONFLICT OF INTEREST

The authors have no conflicts of interest to declare.

REFERENCES

Abbas, H., & Comeau, L. (2003). Aroma synthesis by immobilized lipase from Mucor sp. *Enzyme and Microbial Technology*, *32*(5), 589-595. https://doi.org/10.1016/S0141-0229(03)00022-X

Anand, A., & Weatherley, L. R. (2018). The performance of microbial lipase immobilized onto polyolefin supports for hydrolysis of high oleate sunflower oil. *Process Biochemistry*, *68*, 100-107. https://doi.org/10.1016/j.procbio.2018.01.027

Arroyo, M. (1998). Inmovilización de enzimas. Fundamentos, métodos y aplicaciones. *Ars Pharmaceutica*, *39*(2), 23-39. https://www.ugr.es/~ars/abstract/arroyo.pdf

Bhuyan, D., Selvaraj, K., & Saikia, L. (2017). Pd@ SBA-15 nanocomposite catalyst: Synthesis and efficient solvent-free semihydrogenation of phenylacetylene under mild conditions. *Microporous and Mesoporous Materials*, *241*, 266-273. https://doi.org/10.1016/j.micromeso.2016.12.025

Binner, J. G. P., McDermott, A. M., Yin, Y., Sambrook, R. M., & Vaidhyanathan, B. (2006). In situ coagulation moulding: a new route for high quality, net-shape ceramics. *Ceramics international*, *32*(1), 29-35. https://doi.org/10.1016/j.ceramint.2004.12.006

Blanco, R. M., Terreros, P., Fernández-Pérez, M., Otero, C., & Dıaz-González, G. (2004). Functionalization of mesoporous silica for lipase immobilization: characterization of the support and the catalysts. *Journal of Molecular Catalysis B: Enzymatic*, *30*(2), 83-93. https://doi.org/10.1016/j.molcatb.2004.03.012

Bosley, J. A., & Clayton, J. C. (1994). Blueprint for a lipase support: Use of hydrophobic controlled-pore glasses as model systems. *Biotechnology and bioengineering*, *43*(10), 934-938. https://doi.org/10.1002/bit.260431006

Cai, Q., Hu, C., Yang, N., Wang, Q., Wang, J., Pan, H., ... & Ruan, C. (2018). Enhanced activity and stability of industrial lipases immobilized onto spherelike bacterial cellulose. *International journal of biological macromolecules*, *109*, 1174-1181. https://doi.org/10.1016/j.ijbiomac.2017.11.100

Dang, T. P., Dinh, Q. K., Nguyen, H. P., & Vu, A. T. (2010). The synthesis of novel hybrid thiol-functionalized nanostructured SBA-15. *Advances in Natural Sciences: Nanoscience and Nanotechnology*, *1*(3), 035011. https://doi.org/10.1088/2043-6262/1/3/035011

Dosanjh, N. S., & Kaur, J. (2002). Immobilization, stability and esterification studies of a lipase from a Bacillus sp. *Biotechnology and applied biochemistry*, *36*(1), 7-12. https://iubmb.onlinelibrary.wiley.com/doi/pdf/10.1042/BA20010070

Dove, P. M., & Rimstidt, J. D. (1994). Silica-water interactions. *Reviews in Mineralogy and Geochemistry*, *29*(1), 259-308. https://pubs.geoscienceworld.org/msa/rimg/article-abstract/29/1/259/110563/silica-water-interactions?redirectedFrom=fulltext

Fan, Y., & Qian, J. (2010). Lipase catalysis in ionic liquids/supercritical carbon dioxide and its applications. *Journal of Molecular Catalysis B: Enzymatic*, *66*(1-2), 1-7. https://doi.org/10.1016/j.molcatb.2010.03.004

Grajales, D. L., González, L. M., & Villa, A. L. (2017). Catalytic oxidative dehydrogenation of carveol to carvone over the phthalocyanine complex FePcCl16 immobilized on the mesoporous silica SBA-15. *Applied Catalysis A: General*, *541*, 15-24. https://doi.org/10.1016/j.apcata.2017.04.019

Han, Y. J., Watson, J. T., Stucky, G. D., & Butler, A. (2002). Catalytic activity of mesoporous silicate-immobilized chloroperoxidase. *Journal of Molecular Catalysis B: Enzymatic*,*17*(1),1-8.https://doi.org/10.1016/S1381-1177(01)00072-8

Ispas, C., Sokolov, I., & Andreescu, S. (2009). Enzyme-functionalized mesoporous silica for bioanalytical applications. *Analytical and bioanalytical chemistry*, *393* (2),543-554. https://link.springer.com/article/10.1007%2Fs00216-008-2250-2

Lee, J. E., Lee, N., Kim, T., Kim, J., & Hyeon, T. (2011). Multifunctional mesoporous silica nanocomposite nanoparticles for theranostic applications. *Accounts of chemical research*, *44*(10), 893-902. https://pubs.acs.org/doi/ipdf/10.1021/ar2000259

Li, B., Xu, Z., Jing, F., Luo, S., & Chu, W. (2017). Facile one-pot synthesized ordered mesoporous Mg-SBA-15 supported PtSn catalysts for propane dehydrogenation. *Applied Catalysis A: General*, *533*, 17-27. https://doi.org/10.1016/j.apcata.2016.12.026

Li, Y., Du, W., & Liu, D. (2015). Efficient biodiesel production from phospholipids-containing oil: synchronous catalysis with phospholipase and lipase. *Biochemical engineering journal*,*94*,45-49. https://doi.org/10.1016/j.bej.2014.11.001

Lu, A. H., & Schüth, F. (2006). Nanocasting: a versatile strategy for creating nanostructured porous materials. *Advanced Materials*, *18*(14), 1793-1805. https://doi.org/10.1002/adma.200600148

Mateo, C., Palomo, J. M., Fernandez-Lorente, G., Guisan, J. M., & Fernandez-Lafuente, R. (2007). Improvement of enzyme activity, stability and selectivity via immobilization techniques. *Enzyme and microbial technology*, *40*(6), 1451-1463. https://doi.org/10.1016/j.enzmictec.2007.01.018

Nicolás, P., Lassalle, V. L., & Ferreira, M. L. (2017). Quantification of immobilized Candida antarctica lipase B (CALB) using ICP-AES combined with Bradford method. *Enzyme and microbial technology*, *97*, 97-103. https://doi.org/10.1016/j.enzmictec.2016.11.009

Ning, S. F., Li, H. Y., Chen, W., Liu, B., & Chen, S. T. (2005). Effects of surface oxide species and contents on SiC slurry viscosity. *Rare Metals*, *24*(3), 240-245. http://www.airitilibrary.com/Publication/alDetailedMesh?docid=10010521-200509-24-3-240-245-a

Pogorilyi, R. P., Melnyk, I. V., Zub, Y. L., Seisenbaeva, G. A., & Kessler, V. G. (2016). Enzyme immobilization on a nanoadsorbent for improved stability against heavy metal poisoning. *Colloids and Surfaces B: Biointerfaces*, *144*, 135-142. https://doi.org/10.1016/j.colsurfb.2016.04.003

Reis, P., Holmberg, K., Watzke, H., Leser, M. E., & Miller, R. (2009). Lipases at interfaces: a review. *Advances in colloid and interface science*, *147*, 237-250. https://doi.org/10.1016/j.cis.2008.06.001

Rueda, N., Dos Santos, C. S., Rodriguez, M. D., Albuquerque, T. L., Barbosa, O., Torres, R., ... & Fernandez-Lafuente, R. (2016). Reversible immobilization of lipases on octyl-glutamic agarose beads: A mixed adsorption that reinforces enzyme immobilization. *Journal of Molecular Catalysis B: Enzymatic*, *128*, 10-18. https://doi.org/10.1016/j.molcatb.2016.03.002

Sahoo, B., Sahu, S. K., & Pramanik, P. (2011). A novel method for the immobilization of urease on phosphonate grafted iron oxide nanoparticle. *Journal of Molecular Catalysis B: Enzymatic*, *69*(3-4), 95-102. https://doi.org/10.1016/j.molcatb.2011.01.001

Sequeira, C. A. C., & Amaral, L. (2014). Role of Kirkendall effect in diffusion processes in solids. *Transactions of Nonferrous Metals Society of China*, *24*(1), 1-11. https://doi.org/10.1016/S1003-6326(14)63021-1

Sheldon, R. A., & Van Pelt, S. (2013). Enzyme immobilisation in biocatalysis: why, what and how. *Chemical Society Reviews*, *42*(15), 6223-6235. https://pubs.rsc.org/en/content/articlepdf/2013/cs/c3cs60075k

Son, W. J., Choi, J. S., & Ahn, W. S. (2008). Adsorptive removal of carbon dioxide using polyethyleneimine-loaded mesoporous silica materials. *Microporous and Mesoporous Materials*, *113*(1-3), 31-40. https://doi.org/10.1016/j.micromeso.2007.10.049

Sun, H., Han, J., Ding, Y., Li, W., Duan, J., Chen, P., ... & Zheng, X. (2010). One-pot synthesized mesoporous Ca/SBA-15 solid base for transesterification of sunflower oil with methanol. *Applied Catalysis A: General*, *390*(1-2), 26-34. https://doi.org/10.1016/j.apcata.2010.09.030

Taguchi, A., & Schüth, F. (2005). Ordered mesoporous materials in catalysis. *Microporous and mesoporous materials*, *77*(1), 1-45. https://doi.org/10.1016/j.micromeso.2004.06.030

Urrutia, P., Arrieta, R., Alvarez, L., Cardenas, C., Mesa, M., & Wilson, L. (2018). Immobilization of lipases in hydrophobic chitosan for selective hydrolysis of fish oil: The impact of support functionalization on lipase activity, selectivity and stability. *International journal of biological macromolecules*, *108*, 674-686. https://doi.org/10.1016/j.ijbiomac.2017.12.062

Zare, M., Moradi-Shoeili, Z., Ashouri, F., & Bagherzadeh, M. (2017). Heterogeneous SBA-15-supported Oxoperoxomolybdenum (VI) complex for enhanced olefin epoxydation. *Catalysis Communications*, *88*, 9-12. https://doi.org/10.1016/j.catcom.2016.09.025

Zhang, Y., & Binner, J. (2008). Effect of dispersants on the rheology of aqueous silicon carbide suspensions. *Ceramics international*, *34*(6), 1381-1386. https://doi.org/10.1016/j.ceramint.2007.03.030

Zheng, J., Wei, W., Lan, X., Zhang, Y., & Wang, Z. (2018). Fluorescent microplate assay method for high-throughput detection of lipase transesterification activity. *Analytical biochemistry*, *549*, 26-28. https://doi.org/10.1016/j.ab.2018.03.010